
**Separation Science and Technology**
Publication details, including instructions for authors and subscription information:
http://www.informaworld.com/smpp/title~content=t713708471

# Thermal Considerations in Continuous Flow Electrophoresis

Robert J. Naumann[a]; Percy H. Rhodes[a]
[a] SPACE SCIENCE LABORATORY NASA/MARSHALL SPACE FLIGHT CENTER, HUNTSVILLE, ALABAMA

**To cite this Article** Naumann, Robert J. and Rhodes, Percy H.(1984) 'Thermal Considerations in Continuous Flow Electrophoresis', Separation Science and Technology, 19: 1, 51 — 75
**To link to this Article: DOI:** 10.1080/01496398408059938
**URL:** http://dx.doi.org/10.1080/01496398408059938

SEPARATION SCIENCE AND TECHNOLOGY, 19(1), pp. 51-75, 1984

# Thermal Considerations in Continuous Flow Electrophoresis

ROBERT J. NAUMANN and PERCY H. RHODES

SPACE SCIENCE LABORATORY
NASA/MARSHALL SPACE FLIGHT CENTER
HUNTSVILLE, ALABAMA 35812



**Abstract**

Two-dimensional heat flow in a continuous flow electrophoretic chamber is analyzed assuming Poiseuille flow and finite conductivity of the chamber walls. The thermal field can be characterized in terms of several dimensionless parameters which allow the solution to be applied to a wide variety of operating conditions. Since most electrophoretic chambers have a high aspect ratio, heat flow through the edge walls is not a major effect and the two-dimensional model is adequate. A major advantage of using this simplified approach is that analytical solutions can be obtained which provide insights that are difficult to get from three-dimensional numerical approaches. For example, a criterion is developed for determining the maximum power that can be used in machines operated in upflow or downflow configuration. Also it is shown that the actual structure of the flowfield has no effect on the fully developed thermal field. The model is compared with experimental measurements, and the implications of the thermal field on flow disturbances are discussed. Finally, it is demonstrated that a significant improvement in performance as well as in operational stability can be achieved by increasing the conductivity of the walls of the cooling chamber.

## INTRODUCTION

The use of continuous flow electrophoresis (CFE), developed originally by Hannig (*1*) and Strickler (*2*), has gained renewed interest as a method of separation of particles and macromolecules on a preparative scale. Much of this interest arose from the prospect of using the long duration low-gravity environment provided by an orbiting spacecraft to eliminate the buoyancy-driven flows that limited the operation of CFE devices on Earth (*3, 4*). A by-product of this research has been a much more detailed understanding of how



 0149-6395/84/1901-0051$3.50/0

gravitational effects limit the process, which have led to several innovative ideas for improving the design and operation of CFE devices in Earth's gravity (*5, 6*).

One such limitation on the operation of a CFE device is the electric field that can be applied to provide the desired separation. Increasing the field increases the relative separation between species with slightly different electrophoretic mobilities and tends to improve the resolution. However, such an increase also results in additional Joule heating which may lead to buoyancy-driven flow perturbations and may also be injurious to the sample being separated.

Ostrach (*7*) analyzed the perturbations in the base flow from Joule heating in a CFE device operating in a downflow configuration and developed a criterion for the limit of stable operation based on the onset of flow reversal due to buoyancy effects. He concluded that such instabilities could be avoided by operating in an upflow configuration.



Rhodes (*8*) conducted a series of experiments on specially instrumented flow chambers to test this criterion and found that the onset of severe flow instabilities occurred at much lower power levels than predicted by Ostrach. These findings prompted an extensive theoretical investigation by Saville and others (*9–11*). Saville showed that a fully developed flow in a rectangular column with perfectly conducting walls and an inverted thermal gradient (colder fluid above the warmer) has a hydrodynamic instability that occurs at a critical Rayleigh given number by

$$\mathrm{Ra}_c = \frac{\pi^4}{16}(1 + W^{-2})^2 \tag{1}$$

where $W$ is the ratio of the width to thickness of the column. This corresponds to a $\mathrm{Ra}_c \lesssim 6$. The critical Rayleigh number is even lower for the case of partially conducting walls. This means that practically no inverse axial thermal gradient may be tolerated unless the chamber thickness is extremely small ($\lesssim$1 mm). Machines that operate successfully in unit gravity generally utilize gaps of this size to suppress buoyancy-driven convection, but this severely limits their throughput and resolution because of the distortion of the sample stream from wall effects (*12*).

Therefore, it appears to be necessary to avoid inverse thermal gradients along the flow axis in the operation of anything other than CFE devices with extremely narrow channels. There are three possibilities: (a) the machine may be operated in the downflow configuration with the buffer and sample inserted at an elevated temperature and cooled by extracting heat through the walls as the buffer descends; (b) the machine may be operated in an upflow configuration with the buffer and sample inserted at a low temperature and

allowed to warm as it rises through the machine; (c) the machine may be operated in a low-gravity environment in which it becomes indifferent to the axial gradient.

The purpose of this paper is to analyze the thermal profiles in these various configurations in order to determine the relationships required to establish stable operation and to remain within the operational bounds imposed by sample viability and/or machine and buffer requirements.

## ANALYSIS

Consider a fluid flowing between two parallel semi-infinite planes with spacing $2a$. Poiseuille flow is assumed with velocity profile given by

$$v(y) = \frac{3}{2}\bar{v}(1 - y^2), \qquad -1 \leq y \leq 1 \tag{2}$$

where $\bar{v}$ is the mean flow velocity and $y$ is the transverse coordinate normalized by the half-thickness of the gap between the planes.

At $x = 0$, the fluid has uniform temperature $T_0$. As the fluid traverses the channel, heat is being generated within the fluid at the rate of $\sigma E^2$ per unit volume where $E$ is the local electric field and $\sigma$ is the local electrical conductivity of the buffer. Heat is being extracted through the walls at a rate given by

$$\mp k \left(\frac{\partial T(x, y)}{\partial y}\right)_{y=\pm 1} = H(T(x, \pm 1) - T_w) \tag{3}$$

where $k$ is the thermal conductivity of the buffer, $T(x, \pm 1)$ is the temperature of the buffer along the wall, $H$ is a heat transfer coefficient, and $T_w$ is the temperature of the cooling fluid which acts as a heat sink for the external walls.

It is convenient to work in a dimensionless system in which the dimensionless temperature $\theta(x, y) = (T(x, y) - T_w)/(T_1 - T_w)$ where $T_1$ is some upper limit of temperature that can be tolerated by the sample, the buffer, or the apparatus. All dimensions are scaled by the half-width $a$. Assuming constant properties* for the fluid and steady-state conditions, the thermal field is given by the partial differential equation

$$\nabla^2\theta + \frac{a^2\sigma E^2}{k(T_1 - T_w)} = \frac{3}{2}\frac{a\rho c\bar{v}}{k}(1 - y^2)\frac{\partial\theta}{\partial x} \tag{4}$$

where $\rho c/k$ is the thermal diffusivity of the buffer fluid. It is also convenient to introduce a dimensionless power density given by $Q = 1/2a^2\sigma E^2/[k(T_1 - T_w)]$, a Peclet number given by $\mathrm{Pe} = a\rho c\bar{v}/k$, and a Biot number given by $\mathrm{Bi} = aH/k$. The partial differential equation now becomes

$$\nabla^2\theta + 2Q = \frac{3}{2}\,\mathrm{Pe}(1 - y^2)\frac{\partial\theta}{\partial x} \tag{5}$$

with boundary conditions given by

I. $$\theta(0, y) = \theta_0, \qquad \text{for } -1 \le y \le 1$$

II. $$\left[\frac{\partial\theta(x, y)}{\partial y}\right]_{y=1} = -\mathrm{Bi}\theta(x, 1), \qquad \text{for } x \ge 0$$

III. $$\left[\frac{\partial\theta(x, y)}{\partial y}\right]_{y=0} = 0, \qquad \text{for } x \ge 0$$

This is a variation of the classical Graetz problem (*13*) which has received considerable attention in the heat transfer literature. The general solution consistent with the stated boundary conditions may be written

$$\theta(x, y) = Q(1 + 2/\mathrm{Bi} - y^2) + \sum_{n=1}^{\infty} C_n e^{-2\alpha_n^2 x/3\mathrm{Pe}} Y(\alpha_n, y) \tag{6}$$

where

$$Y(\alpha_n, y) = e^{\alpha_n y^2/2}\,{}_1F_1\left[\frac{\alpha_n^3}{9\mathrm{Pe}^2} + \frac{\alpha_n + 1}{4}, \frac{1}{2}; -\alpha_n^2 y\right]$$

and the ${}_1F_1$ denotes the confluent hypergeometric function.

The eigenvalues $\alpha_n$, $n = 1, 2, \ldots$, are determined by the boundary conditions at the wall, i.e.,

$$(\alpha_n + \mathrm{Bi})\,{}_1F_1\left(\frac{\alpha_n^3}{9\mathrm{Pe}^2} + \frac{\alpha_n + 1}{4}, \frac{1}{2}; -\alpha_n\right)$$

*The effects of temperature-dependent properties are discussed in the Appendix.

$$+ {}_1F_1'\left(\frac{\alpha_n^3}{9\mathrm{Pe}^2} + \frac{\alpha_n + 1}{4}, \frac{1}{2}; -\alpha_n\right) = 0 \qquad (7)$$

For a given Bi and Pe the roots $\alpha_n$ are found using modified Newton-Raphson method. The first six roots for various values of Bi and Pe are tabulated in Table 1.

The Fourier coefficients $C_n$ are found from the condition that the fluid is isothermal at the inlet. Agrawal (*14*) and others have pointed out that this condition is not strictly obeyed at low Peclet numbers because thermal conduction from the heated region influences the temperature distribution of the fluid at the inlet. However, in most CFE devices the Peclet numbers

TABLE 1

Roots of

$$(\alpha n + \mathrm{Bi}){}_1F_1\left(\frac{\alpha_n^3}{9\mathrm{Pe}^2} + \frac{\alpha_n + 1}{4}, 1/2; -\alpha_n\right) + {}_1F_1'\left(\frac{\alpha_n^3}{9\mathrm{Pe}^2} + \frac{\alpha_n + 1}{4}, 1/2; -\alpha_n\right) = 0$$

| $n$ | Bi = ∞ | Bi = 10 | Bi = 1 | Bi = 0.1 |
|---|---|---|---|---|
| | | Pe = ∞ | | |
| 1 | 1.6816 | 1.5518 | 1.0000 | 0.3782 |
| 2 | 5.6698 | 5.3977 | 4.6561 | 4.3336 |
| 3 | 9.6682 | 9.3025 | 8.5620 | 8.3334 |
| 4 | 13.6676 | 13.2308 | 12.5158 | 12.3333 |
| 5 | 17.6672 | 17.1730 | 16.4875 | 16.3334 |
| 6 | 21.6682 | 21.1280 | 20.4538 | 20.3166 |
| | | Pe = 10 | | |
| 1 | 1.6698 | 1.5123 | 0.9970 | 0.3780 |
| 2 | 5.2317 | 4.9884 | 4.3286 | 4.0501 |
| 3 | 8.0556 | 7.7367 | 7.1443 | 6.9887 |
| 4 | 10.3415 | 9.9595 | 9.4661 | 9.3730 |
| 5 | 12.2837 | 11.0582 | 11.4665 | 11.4072 |
| 6 | 13.9935 | 13.5439 | 13.2367 | 13.1960 |
| | | Pe = 1 | | |
| 1 | 1.2537 | 1.1804 | 0.8391 | 0.3628 |
| 2 | 2.5173 | 2.4055 | 2.1299 | 2.0358 |
| 3 | 3.3240 | 3.1879 | 2.9952 | 2.9583 |
| 4 | 3.9697 | 3.8218 | 3.6054 | 3.6653 |
| 5 | 4.5242 | 4.3720 | 4.2713 | 4.2583 |
| 6 | 5.0179 | 4.8656 | 4.7881 | 4.7789 |

associated with the base flow are large enough so that this effect is small. Also, the buffer is usually fed into the chamber through a small tube and some mixing takes place near the entrance region. Therefore, it is reasonable to assume isothermal boundary conditions at $x = 0$.

If $\mathrm{Pe} \gg 1$, the functions $Y(\alpha_n, y)$ reduce to

$$Y(\alpha_n, y) \xrightarrow[\mathrm{Pe} \gg 1]{} e^{\alpha_n y^2/2}\, {}_1F_1\left(\frac{\alpha_n + 1}{4}, \frac{1}{2}; -\alpha_n y^2\right)$$

and are solutions to the differential equation

$$\frac{d^2 Y}{dy^2} + \alpha_n^2(1 - y^2)Y = 0$$

In this limit the $Y$'s are orthogonal with respect to the weighting function $(1 - y^2)$; i.e.,

$$\int_0^1 (1 - y^2)Y(\alpha_n, y)Y(\alpha_m, y) = 0, \qquad n \neq m$$

The Fourier coefficients may be found in the conventional manner; i.e.,

$$C_n = \frac{\int_0^1 (1 - y^2)[\theta_0 - (1 - y^2 + 2/\mathrm{Bi})Q]Y(\alpha_n, y)dy}{\int_0^1 (1 - y^2)Y^2(\alpha_n, y)dy} \tag{8}$$

In the general case, however, the $Y(\alpha_n, y)$ functions are not orthogonal and the Fourier coefficients must be found by other methods. For the calculations used in this study, a collocation method similar to the one described in Ref. *15* was used. The interval $0 \leq y \leq 1$ is divided into $M$ discrete points. The solution vector is truncated at $N$ terms ($N \leq M$) and set equal to $\theta_0$ at $x = 0$ at each discrete value for $y$. This results in an overdetermined set of linear simultaneous equations that can be solved for $C_1, C_2, \ldots, C_n$ by the method of least squares.

In order to assess the effect of the structure of the flow on the thermal field, the case of plug flow (no $y$-dependence in the flow velocity) was also analyzed. The $(1 - y^2)$ term in Eq. (5) is replaced by its average value, 2/3.

The P.D.E. may be solved by separation of variables. With the boundary conditions stated previously, the solution is

$$\theta(x, y) = Q(1 + 2/\mathrm{Bi} - y^2) + \sum_{n=1}^{\infty} C_n e^{(\mathrm{Pe} - \sqrt{\mathrm{Pe}^2 + 4\alpha_n^2})x/2} \cos \alpha_n y \tag{9}$$

TABLE 2
Roots of $\alpha_n \tan \alpha_n = \mathrm{Bi}$

| $n$ | $\mathrm{Bi} = \infty$ | $\mathrm{Bi} = 10$ | $\mathrm{Bi} = 1$ | $\mathrm{Bi} = 0.1$ |
|---|---|---|---|---|
| 1 | 1.5708 | 1.4289 | 0.8603 | 0.3111 |
| 2 | 4.7124 | 4.3058 | 3.4256 | 3.1731 |
| 3 | 7.8540 | 7.2281 | 6.4373 | 6.2991 |
| 4 | 10.9956 | 10.2003 | 9.5293 | 9.4354 |
| 5 | 14.1372 | 13.2142 | 12.6453 | 12.5743 |
| 6 | 17.2788 | 16.2594 | 15.7713 | 15.7143 |

the eigenvalues are given by

$$\alpha_n \tan \alpha_n = \mathrm{Bi} \tag{10}$$

and the Fourier coefficients are given by

$$C_n = \frac{2 \sin \alpha_n}{\alpha_n} \left( \frac{1 + \alpha_n^2/\mathrm{Bi}^2}{1 + \alpha_n^2/\mathrm{Bi}^2 + 1/\mathrm{Bi}} \right) \left( \theta_0 - \frac{2Q}{\alpha_n^2} \right) \tag{11}$$

The first six eigenvalues $\alpha_n$ are tabulated in Table 2 for various values of Bi and Pe.



## DISCUSSION

Axial thermal profiles along the centerline are shown in Fig. 1 for fluid entering a chamber with perfectly conducting walls ($\mathrm{Bi} = \infty$) at $\theta_0 = 1$ and no heat generation. Plug flow at various Peclet numbers is compared with Poiseuille flow. It may be seen that for $\mathrm{Pe} \gtrsim 10$ there is little difference in the axial profiles when axial position is scaled by the inverse Peclet number. This follows from the fact that $\alpha_n^3/9\mathrm{Pe}^2 \ll (\alpha_n + 1)/4$ in Eq. (6) and $(\mathrm{Pe} - \sqrt{\mathrm{Pe}^2 + 4\alpha_n^2})x/2 \to -\alpha_n^2 x/\mathrm{Pe}$ in Eq. (9). For $\mathrm{Pe} = 10$, these conditions are fulfilled only for small $n$. However, for higher values of $n$, the exponential terms are rapidly attenuated for $x > 0$. Also note the similarity in the first few eigenvalues for $\mathrm{Pe} = 10$ and $\mathrm{Pe} = \infty$ in Table 1, especially for decreasing Bi. This indicates that the effect of Peclet number becomes less important for partially conducting walls.

Also note that the thermal profiles for Poiseuille flow are not greatly different from those for plug flow even at large Peclet number. At small

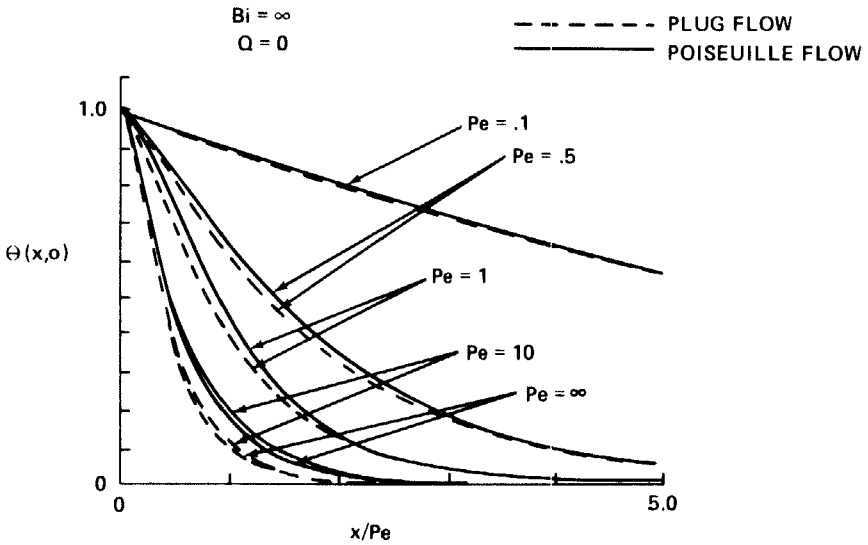


FIG. 1. Comparison of axial thermal profiles computed for Poiseuille flow with plug flow at various Peclet numbers with no heating and perfectly conducting walls. Notice that the plug flow approximation scales very well with $x/\mathrm{Pe}$ for $\mathrm{Pe} \gg 10$, as does Poiseuille flow model. Also notice that thermal profiles for the two models are not greatly different at large Pe. This difference is even less for smaller Pe as conduction in the fluid dominates and the structure of the flow becomes less important.



Peclet numbers, the $\mathrm{Pe}(1 - y^2)$ term becomes small in comparison with other terms, and the difference between the two models is even less.

The similarity is even more pronounced when sample heat is included as may be seen in Figs. 2(a) and 2(b) which show the axial and transverse thermal profiles for $Q = 1$. This also holds for the case of partially conducting walls as may be seen in Fig. 3.

Inspection of the solution of either model reveals that the centerline temperature of the buffer for $x \to \infty$ will be given by $\theta(x, 0) \to (1 + 2/\mathrm{Bi})Q$. If this is not to exceed the maximum specified operating temperature, it is necessary to restrict $Q < (1 + 2/\mathrm{Bi})^{-1}$. As may be seen in Fig. 3, if the buffer is introduced at elevated temperature, a slight rise in temperature will result before the heat generated internally can be conducted to the walls. Therefore, it is necessary to introduce the buffer at slightly below the maximum operating temperature in order to allow for this rise. The maximum temperature is reached at a small fraction of a scale length

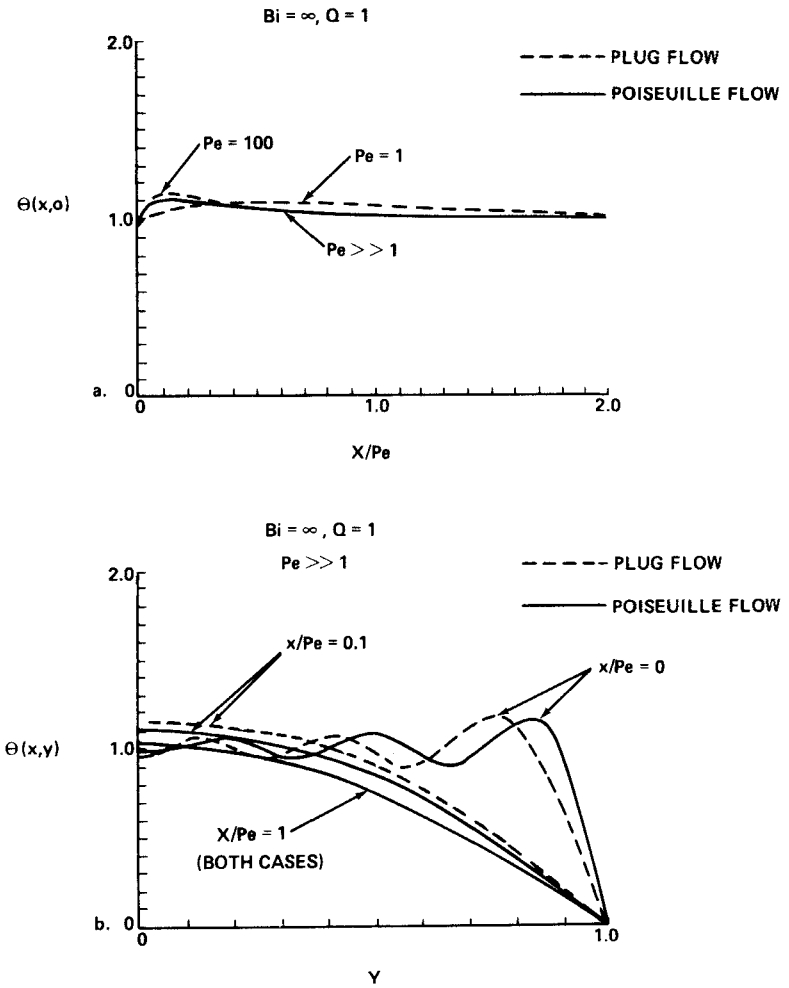


FIG. 2. Axial and transverse thermal profiles for perfectly conducting walls and scaled power dissipation $Q = 1$. In this case there is practically no difference between the two models for $\mathrm{Pe} \gg 1$. Only the first six terms were used to compute the profiles as may be seen by the sinusoidal variations in the $x/\mathrm{Pe} = 0$ profile. These quickly damp out as may be seen for $x/\mathrm{Pe} = 0.1$ and larger.

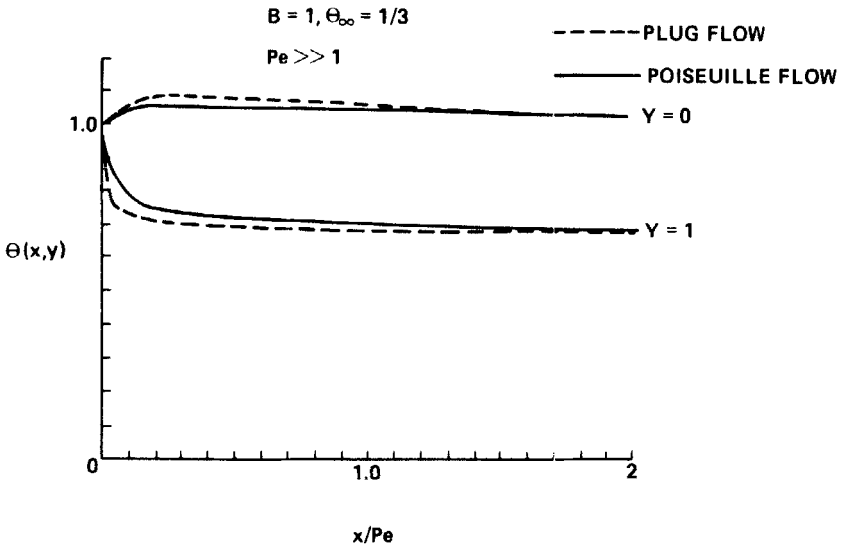


FIG. 3. Comparison of thermal profiles computed for Poiseuille flow and plug flow models for partially conducting walls.



(chamber thickness times the Peclet number), and a small negative thermal gradient exists along the remainder of the chamber. (This would be a stabilizing gradient in a downflow configuration.) The maximum inlet temperature, position of the thermal maximum, and the maximum allowable power dissipation are tabulated in Table 3. Figure 4 shows the resulting thermal profiles for Bi $= \infty$, 10, 1, 0.1.

For machines operated in the upflow configuration it is advantageous to introduce the buffer at the low temperature extreme ($\theta_0 = 0$) and allow it to

TABLE 3
Conditions for Maximum Power Operation in Downflow Configuration

| Bi | Maximum inlet temperature ($\theta_0$) | Maximum power ($Q$) | Position of temperature maximum ($x$/Pe) |
|---|---|---|---|
| 0.1 | 0.9911 | 0.0472 | 0.40 |
| 1.0 | 0.9490 | 0.3162 | 0.25 |
| 10 | 0.9040 | 0.7533 | 0.15 |
| $\infty$ | 0.8974 | 0.8974 | 0.15 |

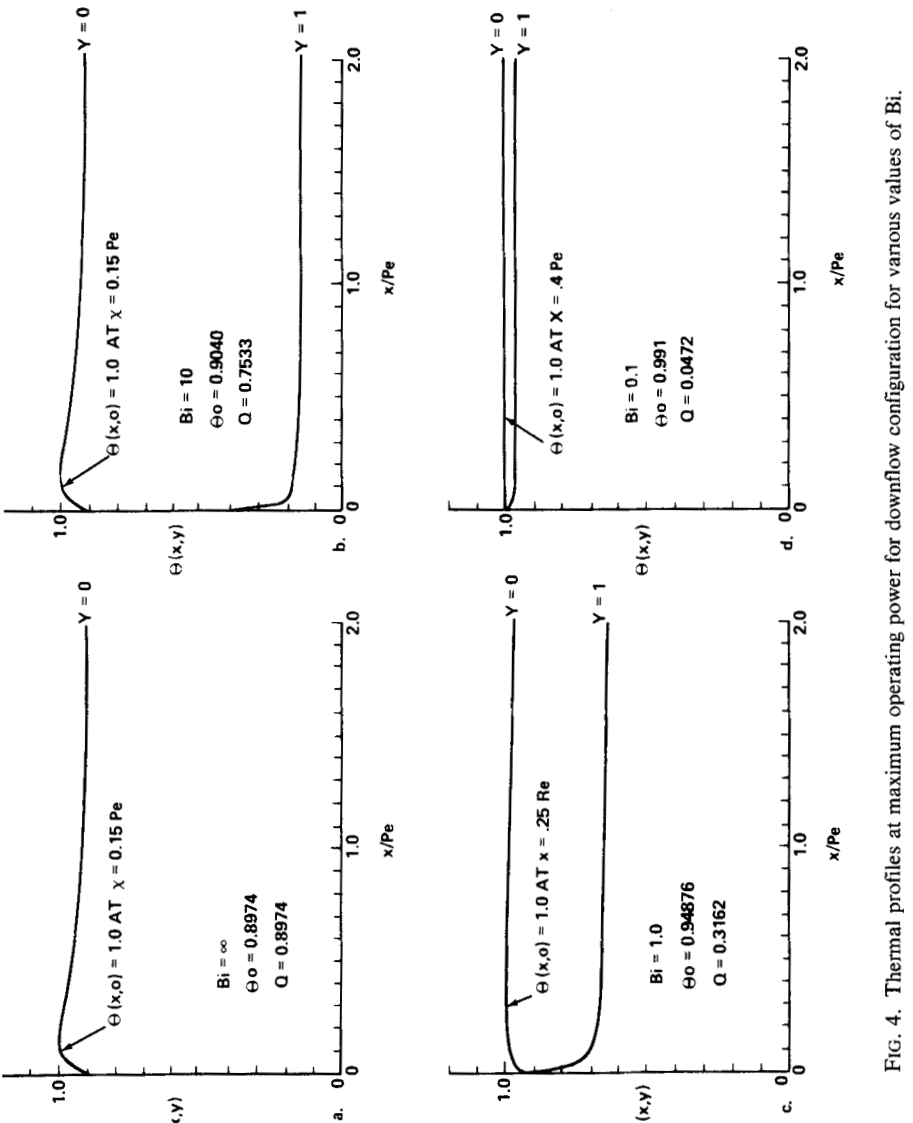


FIG. 4. Thermal profiles at maximum operating power for downflow configuration for various values of Bi.

TABLE 4
Conditions for Maximum Power Operation in Upflow Configuration

| Bi | Maximum power ($Q$) | 1.1 × maximum power ($Q$) | Maximum length for operation at 1.1 × maximum power ($x$/Pe) |
|---|---|---|---|
| 0.1 | 0.0476 | 0.0524 | 25.20 |
| 1.0 | 0.3333 | 0.3667 | 3.65 |
| 10 | 0.8333 | 0.9167 | 1.55 |
| $\infty$ | 1.000 | 1.100 | 1.30 |

warm as it rises. Again the temperature will eventually reach $(1 + 2/\mathrm{Bi})Q$ as $x \to \infty$. Hence, it is necessary to restrict the power dissipation so that $Q < (1 + 2/\mathrm{Bi})^{-1}$ or to restrict the length of the chamber to a value of $x$ such that $\theta(x, 0) < 1$. Table 4 shows the critical power dissipation and the distance in scaled units at which $\theta(x, 0) = 1$ for a fluid inserted at $\theta_0 = 0$ and heated at 1.1 times the critical value of $Q$ for various values of Bi. It may be seen that there is only a slight advantage from the point of view of allowable power dissipation in operating a CFE machine in the upflow configuration. The downflow configuration is penalized only by the small amount of heating in the entrance region which is generally less than 10%. Attempting to operate only 10% above the critical power level in the upflow configuration would greatly restrict the length of the chamber in which separation takes place, which significantly reduces the residence time and the relative separation. For example, if $\mathrm{Bi} = 1$ and $\mathrm{Pe} = 20$, the maximum temperature would be exceeded in 36.5 chamber thicknesses if the power was increased by only 10% above the maximum allowed for steady-state operation. This would restrict the operating length to a few centimeters. It is clear that the most significant gain in performance lies in improving the heat transfer through the walls of the chamber, especially if the Biot number is less than unity. This holds whether the chamber is to be operated in upflow, in downflow, or in low-gravity.

Figures 5 and 6 compare the isotherms near the entrance region for a machine operated in the upflow vs downflow configuration. It may be noted that the downflow configuration offers a much more uniform thermal environment than the upflow configuration. It is interesting to note the structure of the isotherms near the entrance region in the upflow configuration. These peculiar kinks are caused by the fact that the fluid is injected at the wall cooling temperature. Therefore the temperature of the slower moving fluid near the wall must rise from Joule heating before the heat can be

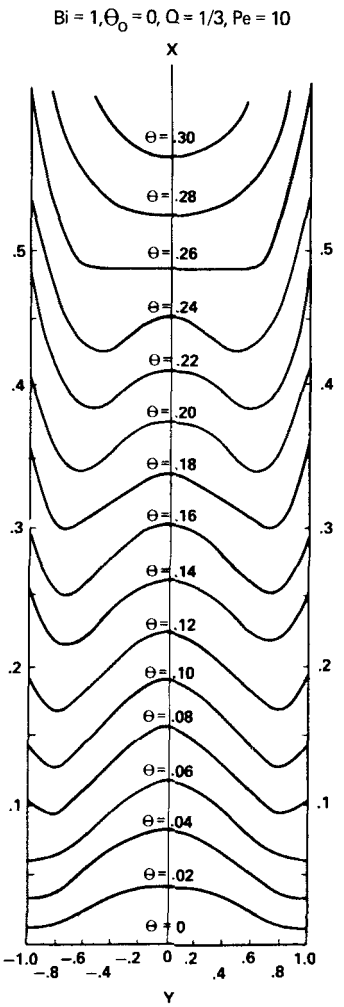


FIG. 5. Isotherms in the entrance of flow channel for up-flow configuration with buffer introduced at $\theta_0 = 0$. A value Pe = 10 was chosen to expand the vertical scale in order to show details of the isotherms. The kinks are caused by the faster-moving cold fluid penetrating into the channel while the slower fluid near the walls has more time to warm from joule heating. Eventually these kinks disappear, and the isotherms become nearly parallel to the walls.

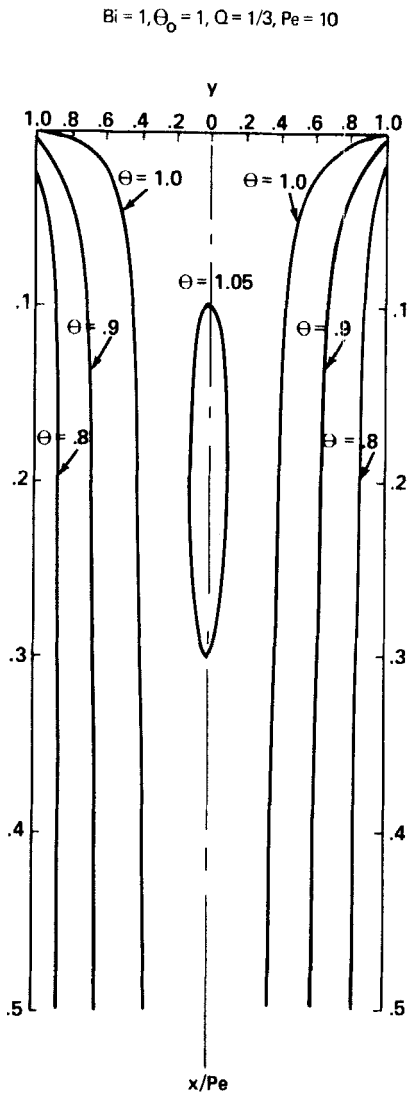


FIG. 6. Isotherms in the entrance region of the flow channel in the downflow configuration for buffer introduced at $\theta_0 = 1.0$. Note region where temperature exceeds 1.

conducted through the wall, whereas the faster moving fluid near the centerline penetrates deeper into the channel before it warms to the same degree. Eventually these kinks disappear and the isotherms become nearly parallel to the flow chamber, resembling the case of purely conductive heat transfer.

A similar effect occurs for the same reason in the vicinity of the end walls in the three-dimensional treatment of the problem by Lynch and Saville (*16*). The simplified two-dimensional model presented in this work ignores the effects of heat conduction and flow modification at the end walls and therefore applies only to the region near the center of CFE devices with high aspect ratio flow chambers. This is the region of maximum temperature for all cases except the one just noted, and therefore the two-dimensional model is adequate for estimating operational limits for most CFE devices.



## COMPARISON WITH EXPERIMENTAL DATA

A series of experiments was conducted using a specially instrumented test chamber. The chamber faces are 0.2 cm thick. The electrodes are Cu strips 18.1 cm long and are mounted on the edge walls. The entire chamber is jacketed, and coolant is pumped through the jacket from bottom to top to provide heat extraction.

Buffer enters the top of the chamber and flows downward at a nominal rate of 19 mL/min. Five marker streams of latex particles are also injected near the top of the chamber to visualize any disturbances in the flow field. Five thermistors are located along the center line of one of the chamber faces to monitor temperature at various points along the flow channel. These thermistors can be moved in and out to profile the temperature field across the thickness of the flow channel. Power in the form of 400 Hz ac is used to study the effects of buffer heating without the complicating effects of electroosmotic flow.

Taking the thermal conductivity of the Plexiglas chamber faces as $2.16 \times 10^{-3}$ W/cm/K, the half-width as $a = 0.25$ cm, and the buffer thermal conductivity as $5.82 \times 10^{-3}$ W/cm/K, the Biot number is $\mathrm{Bi} = 0.464$. The nominal Peclet number is 22.74.

In the first set of runs shown in Fig. 7, the inlet temperature of the buffer was nominally 22.3°C, and the coolant was nominally 16°C at the inlet. A rise of approximately 0.6°C was noted as the coolant fluid traversed the chamber. The average coolant temperature was used to compute the dimensionless temperature and power dissipation.

The agreement between the measured and calculated thermal profiles is quite good, particularly for the low power runs. The error bars on the

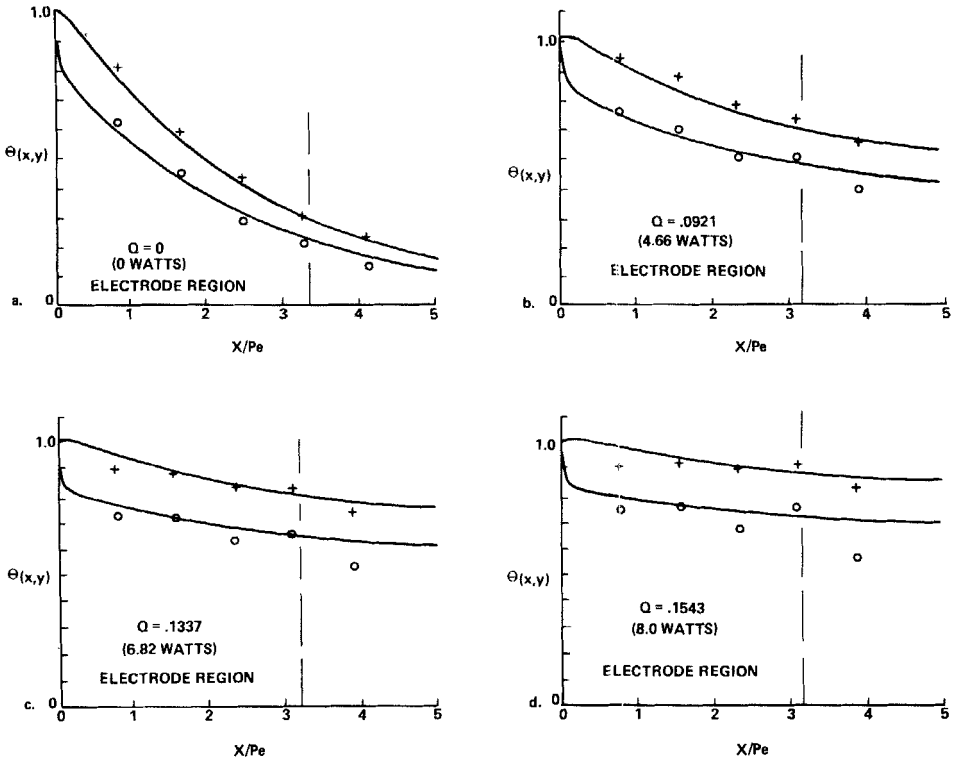


FIG. 7. Comparison of calculated thermal profiles with experimental measurements for downflow configuration with buffer introduced 6°C above the wall temperature. As power is increased, the last data point deviates from the model because it is beyond the electrode region where heating is taking place. Also note the adverse gradient developing between the third and fourth data points. This is probably caused by inhomogeneities in the coolant circulation and poorly conducting walls that can support lateral gradients.

temperature measurements reflect the ±0.05°C accuracy of the thermistor calibration and data acquisition system. The last thermistor reading is slightly below the calculated flow temperature. This is because the model assumes the electrodes continue throughout the chamber whereas, in the actual chamber, they terminate at the thermistor 4 location. This allows the buffer to cool somewhat more than predicated by the model before it reaches the last thermistor.

The flow field is perfectly rectilinear for the case of zero power. As the power is increased, some flow distortion becomes apparent. The sample streams begin to deflect and form kinks. The circular cross section becomes ribbonlike and starts to twist. No flow reversal has yet occurred; the observed disturbances appear to be related to flow perturbations caused by nonuniform cooling of the chamber walls. Since the chamber walls are relatively poor conductors, they can sustain lateral thermal gradients resulting from unequal flow of the coolant. Finally, at the highest power setting a small inverse axial gradient does occur between the third and fourth thermistor and flow reversal results, as predicted by the Saville stability analysis. This occurs at a power level that should still provide a monotonic decreasing axial temperature profile according to the thermal model. The average of the actual data follows the thermal model reasonably well even at these higher power settings, but apparently local cooling inhomogeneities can permit small variations around the average temperature profile which can produce severe flow instabilities.

Figure 8 shows a similar set of data except that the coolant temperature was lowered to approximately 12°C below the buffer inlet temperature. This provides more heat extraction and allows operation at higher power levels. However, the results, when plotted in dimensionless coordinates, are virtually identical with those shown in Fig. 7. The same adverse gradient begins developing between the third and fourth thermistor at about the same scaled power level and flow reversal results.



## SUMMARY

A two-dimensional model for the temperature field in the buffer flowing in a continuous flow electrophoretic chamber has been developed by solving the classical Graetz problem. A simplified analysis assuming plug flow was also included for comparison in order to assess the importance of the flow structure on the thermal field. The results of the two models differ only in the entrance region and converge to the same form after a few scale lengths, which indicates that the transverse structure of the flow field is of no consequence to the thermal field in the fully developed region. This is useful because in actual practice the Poiseuille flow field will be distorted by buoyancy effects. Good agreement between the model and actual flow experiments was obtained. The average trend of the thermal data is predicted quite accurately, but some variations about the predicted values are observed which are probably due to inhomogeneities in the coolant flow.

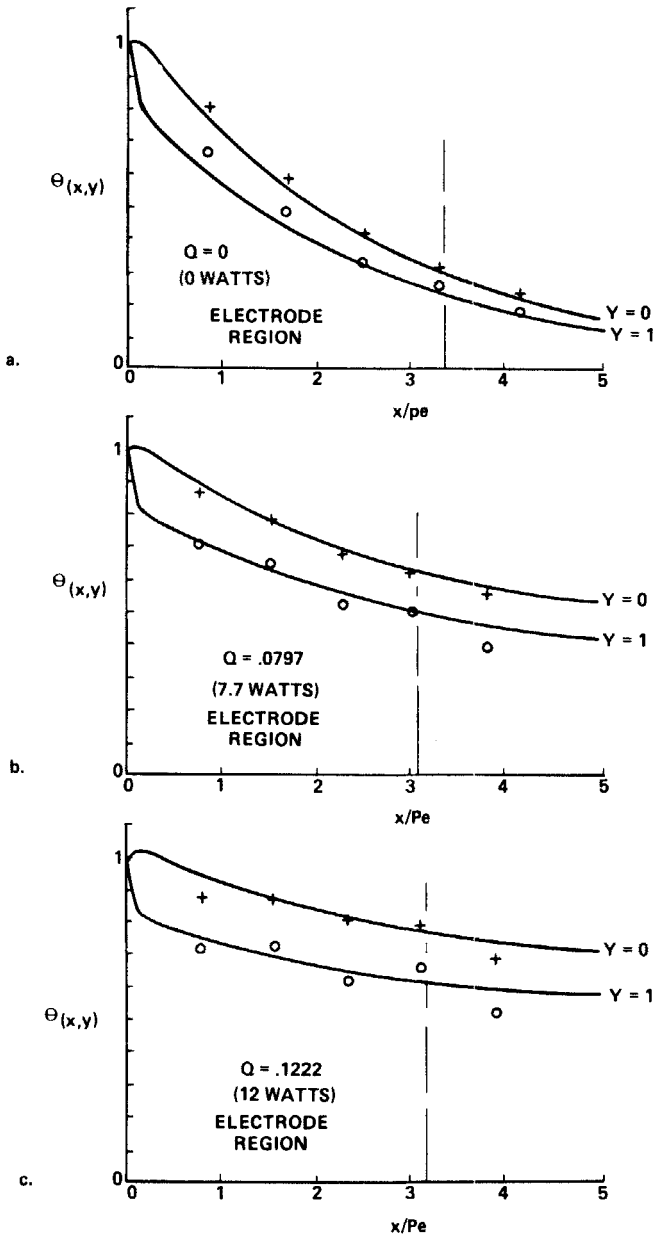


FIG. 8. Comparison of calculated thermal profiles with experimental measurements with the buffer introduced 12°C below the wall temperature. The behavior is quite similar to Fig. 7, indicating that the scaling in the model holds extremely well.

Both models predict a center line temperature at large axial distances given by

$$T - T_w = \left(\frac{1}{2} + \frac{1}{\text{Bi}}\right)\frac{a^2 E^2 \sigma}{k}$$

where $T_w$ is the cooling wall temperature, $E^2\sigma$ is the average power density from Joule heating, $k$ is the thermal conductivity of the buffer, $a$ is the chamber half-thickness, and Bi is the Biot number. If there is some maximum temperature that can be tolerated by the machine, buffer, or sample, this relation sets the upper limit on power density that can be used. The use of transparent walls, which are generally poor conductors, results in Biot numbers substantially less than unity, which greatly restricts the operating power level. Use of conductive walls with thin insulating coatings can increase the Biot number to well above unity. This will be a necessity for wide-gap machines considered for use in low gravity because of the $a^2$ term in the numerator.



Downflow machines can in principle be operated near the limit given by the previous expression without encountering adverse gradients (except for a short distance from the entrance region) provided the buffer is introduced at temperatures near the upper limit. However, the stabilizing gradient is much lower in this configuration than it would be if the buffer were introduced at the wall temperature and allowed to warm as in the upflow configuration. It may be necessary to further reduce the power level to achieve a more favorable stabilizing gradient to prevent excessive flow distortions. Also, the use of insulating walls that can support lateral thermal gradients may lead to severe perturbations in the flow field if there are any inhomogeneities in the cooling system.

In both cases the autothermal effect (increased heating because of the variation of electrical conductance with temperature) can be significant, especially for large Biot numbers as shown in the Appendix. A correction in the maximum operating conditions must be made to stay within operating limits. These corrections are modest (5% reduction in applied field or 10% reduction in power level under worst case conditions) but essential. Failure to consider these corrections can result in temperatures 25% higher than predicted by the constant properties model using average values.

It should also be remembered that a two-dimensional model such as developed in this work is restricted to the center region of a large aspect ratio flow chamber. Heat transfer and flow effects from the end walls can produce additional perturbations to the thermal field several chamber thicknesses into the channel. The two-dimensional treatment is useful for assessing the

maximum operating conditions but may not be adequate for detailed thermal modeling across the entire chamber.

## APPENDIX

### Effects of Variable Electrical Conductivity

Since the electrical conductance* of the buffer fluid used in CFE devices can vary significantly with temperature, it is important to assess the influence of this effect on the thermal profile and operating limits of such devices. Assume this variation is linear in temperature over the range of interest and can be expressed by

$$\sigma(\theta) = \sigma_w(1 + \sigma_1\theta) \tag{A1}$$

where $\sigma_w$ is the conductance at $\theta = 0$ and

$$\sigma_1 = (T_1 - T_w)\frac{1}{\sigma_w}\left(\frac{\partial\sigma}{\partial T}\right)_{T_w} \tag{A2}$$

The inhomogeneous part of Eq. (5) can be written

$$\frac{d^2\theta_i}{dy^2} + \frac{a^2\sigma_w E^2(1 + \sigma_1\theta)}{k(T_1 - T_w)} = 0 \tag{A3}$$

The solution consistent with the previously stated boundary conditions can be obtained using Laplace transforms:

$$\theta i(y) = \left\{\frac{\text{Bi} \cos(\sqrt{A_2\sigma_1}y)}{\text{Bi} \cos\sqrt{A_2\sigma_1} - \sqrt{A_2\sigma_1}\sin\sqrt{A_2\sigma_1}} - 1\right\}\frac{1}{\sigma_1} \tag{A4}$$

where

$$A_2 = \frac{a^2\sigma_w E_2^2}{k(T_1 - T_w)}$$

*Other physical properties of the buffer, such as thermal conductivity and viscosity, also vary with temperature, but the variation of electrical conductance greatly exceeds the other variations.

As $\sigma_1 \to 0$, this expression reduces to the constant property model

$$\theta i(y) = \frac{a^2 <\sigma> E_1^2}{2k(T_1 - T_w)} (1 + 2/\mathrm{Bi} - y^2) = Q(1 + 2/\mathrm{Bi} - y^2) \quad (A5)$$

Here $<\sigma>$ is the average conductance of the buffer given by $\sigma_w(1 + \sigma_1 <\theta>)$, and $<\theta>$ is the average temperature given by

$$<\theta> = \int_0^1 \theta(y)dy = \frac{2}{3}\left(\frac{\mathrm{Bi} + 3}{\mathrm{Bi} + 2}\right) \quad (A6)$$

The subscripts 1 and 2 denote the applied electric fields for the case of constant physical properties and temperature-dependent electrical conductance, respectively.

The conductance of a typical buffer can be described by

$$\sigma(T) = 218 + 8.7T\ (^\circ\mathrm{C})\ (\mu\mathrm{S/cm}) \quad (A7)$$

over the range from 4 to 34°C. Taking this as the maximum operating range for any CFE device, $\sigma_1 = 1.26$.

The two models were compared first by choosing the maximum field $E_1$ allowed by the constant property model, given by

$$E_1^2 = \frac{k(T_1 - T_w)}{a^2 \sigma_w (1 + \sigma_1 <\theta>)} \left(\frac{2}{1 + 2/\mathrm{Bi}}\right)$$

and setting $E^2$ in the variable property model to this value, i.e.,

$$A_2 = \frac{a^2 \sigma_w E_1^2}{k(T_1 - T_w)} = \frac{2}{1 + 2/\mathrm{Bi}} \left(\frac{1}{1 + \sigma_1 <\theta>}\right)$$

The results are shown in Fig. A1. There is little difference between the two models for $\mathrm{Bi} \lesssim 1$. For larger Biot numbers there would be a significant rise (as much as 26%) in centerline temperature if the actual device were operated at the fields computed from the constant property model. Figure A2 shows the results of exceeding the critical field given by

$$E_c^2 = \frac{2k(T_1 - T_w)}{a^2 <\sigma> (1 + 2/\mathrm{Bi})}$$

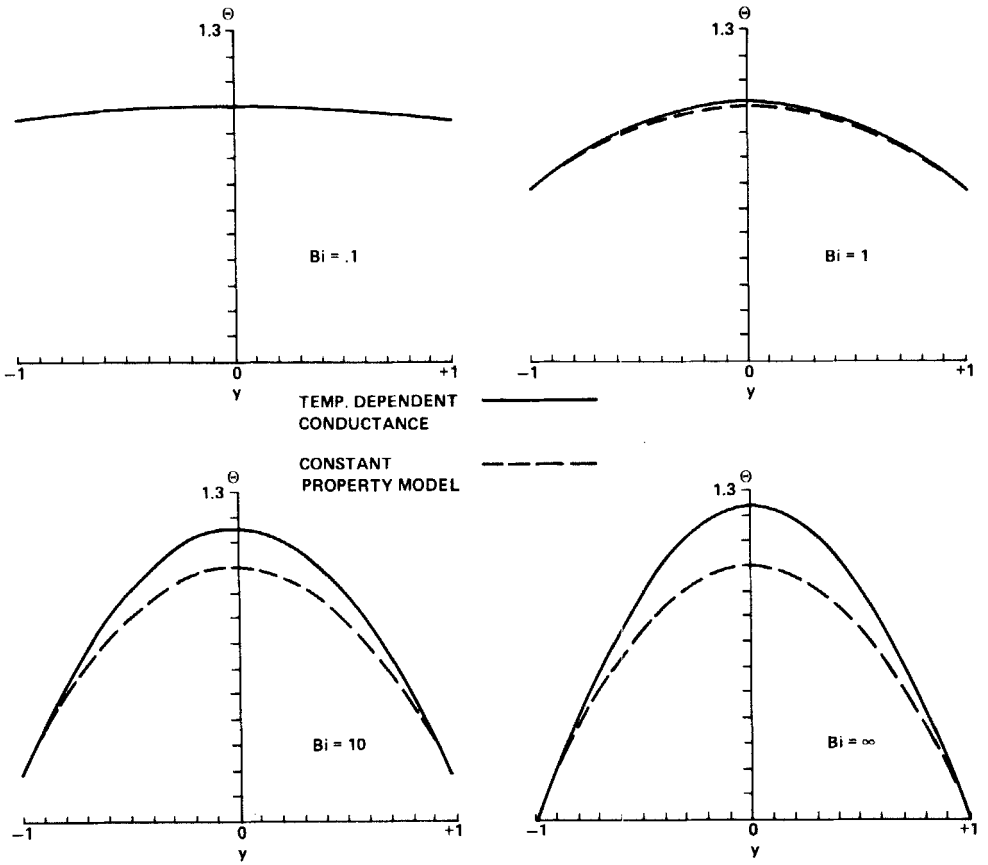


FIG. A1. Thermal profiles from autothermal effect obtained by operating at the maximum critical power permitted by the constant property model.

If it is desired to keep the buffer below $\theta = 1$, it is necessary to operate at a lower applied field. The amount of reduction required is found by setting $\theta_1(0) = 1$ in Eq. (A4) and solving for $A_2$ by the Newton-Raphson method. The corresponding field strength $E_2$ is found from

$$E_2^2 = \frac{A_2 k(T_1 - T_w)}{a^2 \sigma_w}$$

or the ratio of $E_2$ to $E_1$ is given by

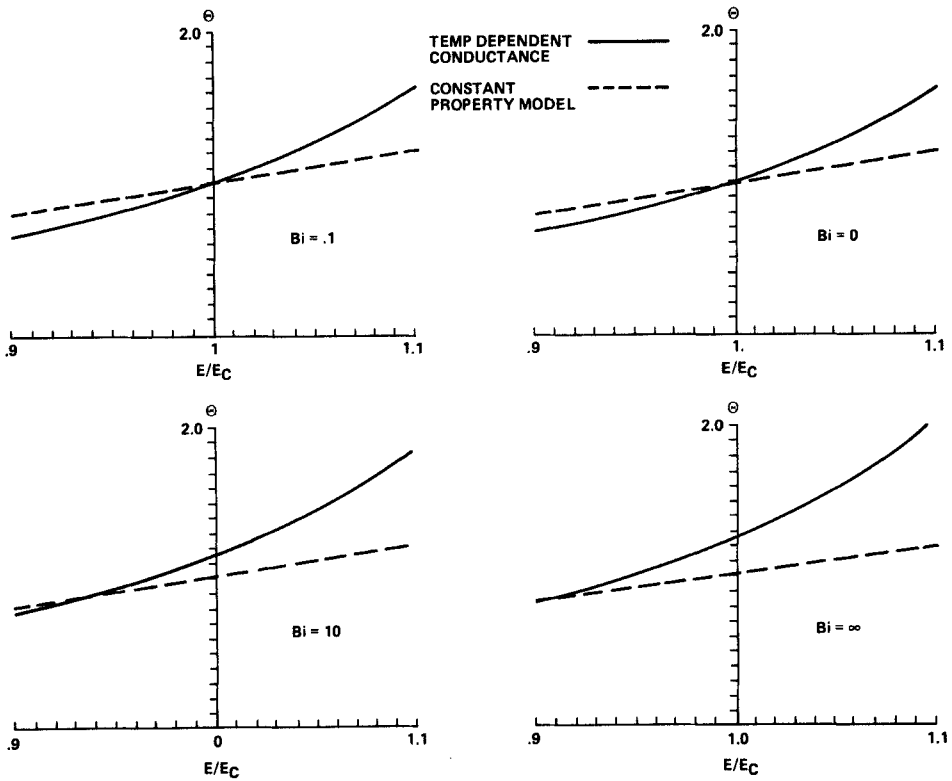


FIG. A2. Centerline temperature from autothermal effect as a function of applied field compared with predictions from constant property model. The critical field, $E_c$, is that field which results in $\theta(x, 0) = 1$ using the constant property model.

$$\frac{E_2^2}{E_1^2} = A_2 \left( \frac{1 + 2/\mathrm{Bi}}{2} \right) (1 + \sigma_1 \langle \theta \rangle)$$

This correction in maximum operating field strength is shown in Fig. A3 as a function of reciprocal Biot number. Note that the maximum correction required as $\mathrm{Bi} \to \infty$ is only 5%. The resulting thermal profiles using this correction factor are shown in Fig. A4. It may be seen that the thermal profiles from either model are now virtually identical, even for the large Biot numbers.

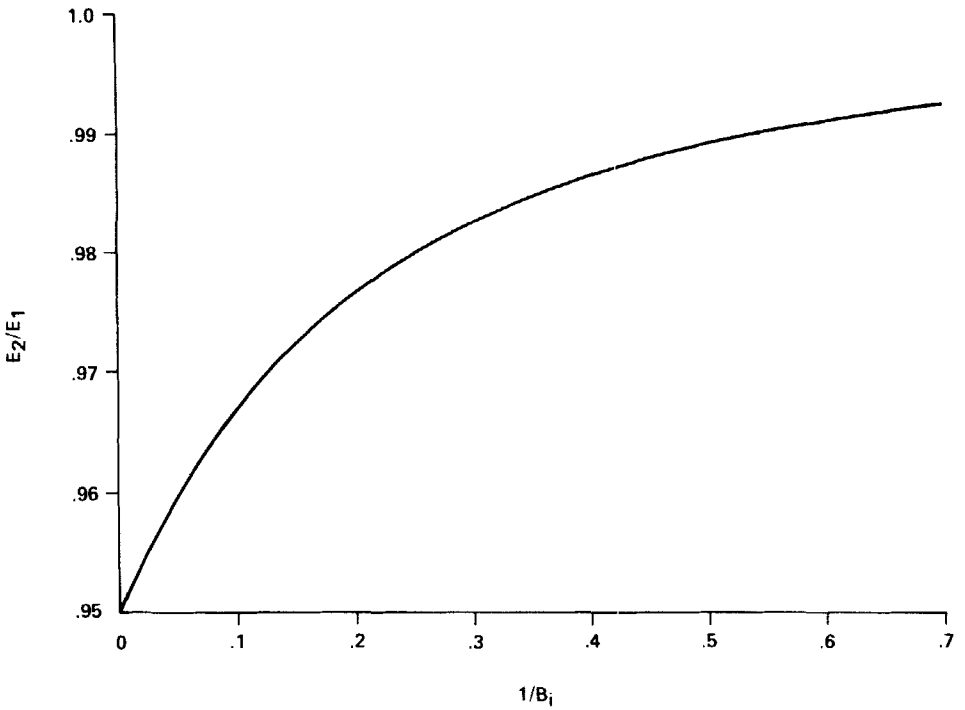


FIG. A3. Reduction factor in applied field required to account for the autothermal effect as a function of reciprocal Biot number. Note that for the worst case ($Bi = \infty$) the applied field must be reduced by only 5% below the critical value predicted from the constant property model.



It may therefore be concluded that average physical properties can be used with little error except in cases of large Biot numbers. Even in the most extreme case the only correction required is a reduction of less than 5% in the maximum applied field.

## REFERENCES

1. K. Hannig, *Z. Anal. Chem., 181,* 244 (1961).
2. A. Strickler, *Sep. Sci., 2,* 335 (1967).
3. P. H. Rhodes, "High Resolution Continuous-Flow Electrophoresis in the Reduced Gravity Environment," in *Electrophonesis 81* (R. C. Allen and P. Arnaud, (eds.), de Gruyter, Berlin, 1981, pp. 919–932.
4. Joint Endeavor Agreement between McDonnell Douglas Astronautics Corporation and NASA in the area of materials processing in space, 1979.
5. P. H. Rhodes and R. S. Snyder, U.S. Patent 4,349,249 (September 14, 1982).

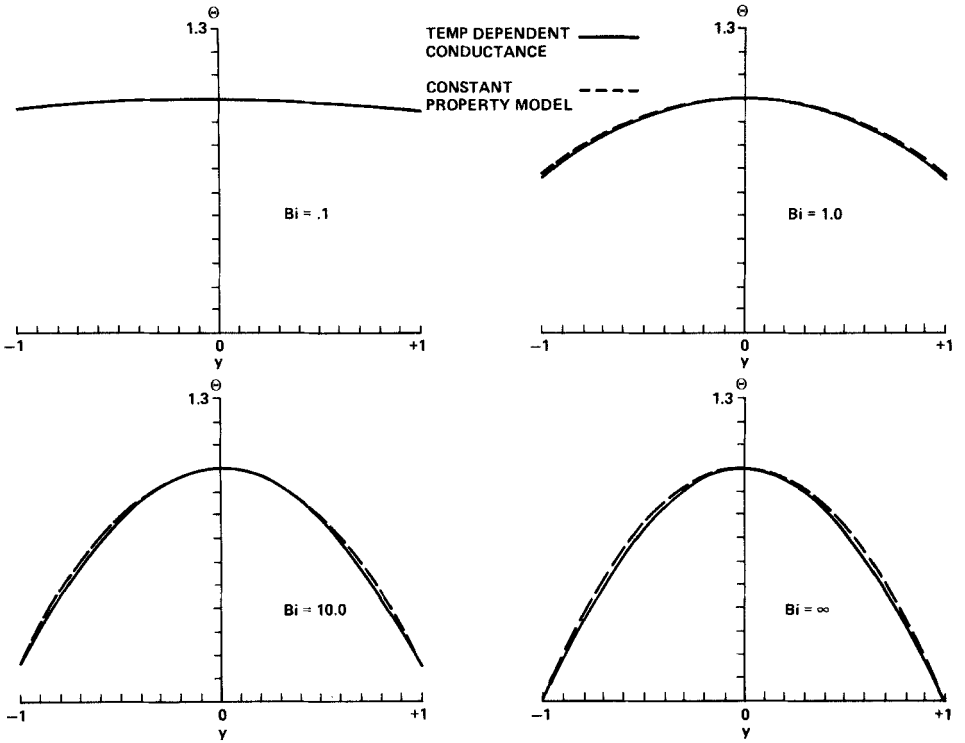


FIG. A4. Thermal profiles with applied field reduced to account for the autothermal effect. Note that the resulting profiles are very similar to those predicted by the constant property model.




6. P. H. Rhodes, U.S. Patent 4,358,358 (November 9, 1982).
7. S. Ostrach, *J. Chromatogr., 140*, 187–195 (1977).
8. P. H. Rhodes, *NASA TM-78178*, Marshall Space Flight Center, August 1979.
9. D. A. Saville, "Fluid Mechanics of Continuous Flow Electrophoresis," in (COSPAR) *Space Research*, Vol. XIX (M. J. Rycroft, ed.), Pergamon, Oxford, 1979, pp. 583–597.
10. D. A. Saville, *Physicochem. Hydrodynamics, 1*, 297–308 (1980).
11. D. A. Saville and J. Dieber, "Flow Structure in Continuous Flow Electrophoresis," in *Materials Research Society Symposia Proceedings*, Vol. 9 (G. Rindone, ed.), Elsevier, New York, 1982, pp. 217–223.
12. A. Strickler and T. Sacks, *Ann. N.Y. Acad. Sci., 209*, 497 (1973).
13. L. Graetz, *Ann. Phys., 25*, 337 (1885).
14. H. C. Agrawal, *Appl. Sci. Res., A9*, 177 (1960).
15. R. J. Naumann, *J. Crystal Growth, 58*, 554 (1982).
16. E. D. Lynch and D. A. Saville, *Chem. Eng. Commun., 9*, 201 (1981).


*Received by editor July 5, 1983*